Journal of
Materials Chemistry A

ROYAL SOCIETY OF CHEMISTRY

PAPER

View Article Online
View Journal | View Issue

Check for updates

Cite this: *J. Mater. Chem. A*, 2022, **10**, 20101

Electropolymerized thin films with a microporous architecture enabling molecular sieving in harsh organic solvents under high temperature†

Yanqiu Lu,[a] Wei Liu,[b] Kaiyu Wang[a] and Sui Zhang *[a]

Received 19th March 2022
Accepted 2nd August 2022

DOI: 10.1039/d2ta02178a

rsc.li/materials-a

Engineering membranes for precise molecular sieving in harsh organic solvents offer unprecedented opportunities for widening the application of organic solvent nanofiltration (OSN). Here, we introduce tris(4-carbazoyl-9-ylphenyl)amine (TCTA) as the monomer to form robust conjugated microporous polymer (CMP) membranes *via* electrochemical polymerization for OSN in a challenging environment. The method enables the use of rigid CMP membranes in harsh dimethylformamide (DMF) with temperature up to 100 °C. The resulting membranes show size-dependent selectivity towards charged dyes and pharmaceutical molecules. Moreover, the membranes present excellent stability in DMF solution containing a high base content of triethylamine at different temperatures due to their rigid crosslinked chemical structure. The optimal membrane can reach 94.4 ± 2.2% rejection of Allura Red AC (496.42 g mol^{-1}) at a dimethylformamide (DMF) permeance of 33.1 ± 1.2 L m^{-2} h^{-1} bar^{-1} at 100 °C. To the best of our knowledge, this is the first report to experimentally recognize the unique advantages of CMPs in high-temperature OSN applications.

1. Introduction

The fine chemical and pharmaceutical industries manufacture a large amount of consumer products and pharmaceuticals, which involves a high volume of organic solvents.[1–3] Large quantities of organic solvent waste are generated during these manufacturing processes. Organic solvents account for 80% of wastes generated by typical pharmaceutical processes,[2,4] placing a huge burden on the environment and operating costs. Surging demands for separation and the stringent environmental laws have driven greener separation methods to replace traditional technologies such as distillation, extraction and adsorption.[5] Organic solvent nanofiltration (OSN) employing membranes for molecular-level separation from organic solvents is an alternative approach that usually requires less footprint and is more environmentally benign.[6–8] However, similar to other membrane-based separation processes, OSN suffers from the trade-off between selectivity and permeability due to the limited porosity and the inherent non-uniform pore structure in most membranes.[9,10] Therefore, the precise tuning of the pore aperture at the nanoscale and the increase of the porosity are still in high demand to enable effective molecular separation. Another key challenge of OSN is the membrane stability in harsh organic solvents, especially polar aprotic solvents (PASs), which are widely used to dissolve active pharmaceutical ingredients (APIs), owing to their midrange lipophilicity.[11] However, the toxicity of most PASs is of great concern and the recovery of PASs is highly desirable to avoid environmental pollution. Currently, most commercially available OSN membranes are made from

Dr Sui Zhang is an Assistant Professor in the Department of Chemical and Biomolecular Engineering, National University of Singapore (NUS). She received her Bachelor's degree from Fudan University in Jun 2008, and her PhD degree from NUS in Dec 2012. Then she did postdoctoral research at NUS and the Massachusetts Institute of Technology before joining NUS in Oct 2017. She started her journey into the membrane field since her PhD studies and has built increasing interest in it since then. She is particularly interested in membranes made from emerging materials with well controlled transport pathways such as 2D materials and microporous polymers.

---

[a] Department of Chemical and Biomolecular Engineering, National University of Singapore, 4 Engineering Drive 4, Singapore 117585, Singapore. E-mail: chezhasu@nus.edu.sg; chezhangsui@nus.edu.sg; Web: **https://blog.nus.edu.sg/suizhang/**

[b] School of Physics, Frontiers Science Center for Mobile Information Communication and Security, Quantum Information Research Center, Southeast University, Nanjing 211189, China

† Electronic supplementary information (ESI) available. See **https://doi.org/10.1039/d2ta02178a**

glassy polymeric materials.[6,12] The limited stability and aging of these materials in harsh organic solvents can lead to adverse changes in membrane performance, especially at temperatures higher than 90 °C, which are commonly seen in pharmaceutical or fine chemical industries.[13,14] High temperature will further accelerate the aging effects, leading to failures of the membranes.[15–17] Since high-temperature OSN has substantial industrial significance,[12] it is desirable to engineer membranes with high chemical stability under such harsh conditions.

The development of a new class of membrane materials is an important pathway to address the limitations of conventional membranes under industrial conditions. To this end, great efforts have been inspired for the integration of typical porous materials, such as zeolites,[18,19] covalent organic frameworks (COFs),[20–23] metal–organic frameworks (MOFs),[24,25] polymers of intrinsic microporosity (PIMs),[26,27] monolayer graphene,[28–30] and MoS_2 (ref. 31 and 32) into membranes. However, the large-scale fabrication of these materials into defect-free membranes and the stability of their membranes under harsh conditions remain as concerns. Conjugated microporous polymers (CMPs), a type of porous material which combines π-conjugated skeletons, impressive pore uniformity and porosity, have emerged as promising candidates for constructing next-generation membranes for molecular sieving.[33–36] The diversity of active building blocks and functional cores enables the development of a broad variety of CMPs with interesting properties and structures.[37] Moreover, the exceptional chemical and thermal stability of CMPs exceed those of many COFs and MOFs,[38] making them particularly appealing for OSN at high temperature in harsh solvent.

In recent years, attention has been paid to the preparation of CMPs by electrochemical polymerization (EP) to obtain high-quality CMP films.[34,35,39] An important feature of EP is that polymerization occurs on the electrode surface, where organic molecules can be deposited directly to form a thin film, avoiding further processing of CMPs.[40] In addition, it is easy to control the film thickness and film formation process *via* adjusting the electrochemical parameters such as scan rate and cycles. Moreover, EP is an environmentally friendly method that requires no catalysis and the electropolymerization process can be completed in a short time. Though the EP method has some limitations (*e.g.* (1) sensitivity to electrochemical parameters; (2) the monomers used should present electrochemically active sites; (3) the size of the fabricated membrane is limited by the size of the electrode support, *etc.*), it is an effective approach for the fabrication of CMP membranes and provide more opportunities for them in membrane separation. Previous research has reported the electropolymerization of CMPs on fluorine-doped tin oxide (FTO) and the electropolymerized CMP films were peeled off from FTO for gas separation.[39] Tang's group has synthesized CMP films on indium tin oxide (ITO) and the CMP film can be transferred to an arbitrary porous support after etching the ITO surface with diluted HCl solution.[34] Recently, Lai and coworkers reported the electropolymerization of CMPs on carbon nanotubes (CNTs)[41,42] or a polydopamine modified CNT substrate with a highly smooth and porous surface and good adhesion to CMPs.[35] Large-area films can be fabricated by EP using large-area WEs. Previous research has shown large films fabricated by EP with a "star" shape (8.0 cm × 8.0 cm) and a rectangular shape (15.0 cm × 8.5 cm).[43] Though CMPs have been electropolymerized for OSN applications,[34,35] their performances under harsh conditions, *i.e.* harsh DMF solvents at high temperatures, have not yet been reported.

Herein, we report a CMP membrane for high-temperature OSN. The robust CMP membrane was fabricated *via* electropolymerization of tris(4-carbazoyl-9-ylphenyl)amine (TCTA) on the surface of a carbon nanotube (CNT) support (Fig. 1a). Tris(4-carbazoyl-9-ylphenyl)amine (TCTA), which has three carbazole groups and triphenylamine (Fig. 1c), was chosen as the monomer due to its good thermal stability. Multiple carbazole functional groups on TCTA can easily form a microporous polymer network. The impact of electrochemical conditions on membrane properties was studied, and the permeance and rejection of the TCTA-EP membrane were evaluated against a wide range of organic solvents, dyes and pharmaceutical molecules. The membrane demonstrated high DMF permeance and size-based separation, and impressive stability in challenging solutions such as strong acid, base and high-temperature DMF solutions containing a high base content of triethylamine. To the best of our knowledge, the performance of our electropolymerized CMP membrane exceeds that of current reported membranes in DMF at high temperature. This method may open new possibilities for challenging OSN applications under harsh conditions.

2. Experimental section

2.1. Chemicals and materials

Single-walled carbon nanotubes (SWCNTs, diameter: 0.78 nm, (6,5) chirality, median length: 1 μm, ≥95%), tetrabutylammonium perchlorate (electrochemical analysis, ≥99.0%), tris(4-carbazoyl-9-ylphenyl)amine (TCTA, 97%), acetonitrile (HPLC, ≥99.9%), propylene carbonate (HPLC, 99.7%), sodium dodecyl sulfate (SDS, ≥98%), methyl orange (MO, 85%, MW = 327.33 g mol^{-1}), Brilliant Blue R (BBR, ≥70%, MW = 826 g mol^{-1}), rose bengal (RB, 95%, MW = 1017.65 g mol^{-1}), methylene blue (MB, 82%, MW = 319.9 g mol^{-1}), crystal violet (CV, ≥90%, MW = 407.98 g mol^{-1}), Rhodamine 6G (R6G, 95%, MW = 530.0 g mol^{-1}), alcian blue (AB, 45–65%, MW = 1298.86 g mol^{-1}), Sudan IV (SIV, ≥80%, MW = 380.44 g mol^{-1}), tetracycline (≥98%, MW = 444.43 g mol^{-1}), oxytetracycline dihydrate (≥95%, MW = 496.46 g mol^{-1}), vitamin B_{12} (≥98%, MW = 1355.37 g mol^{-1}), and potassium iodide (≥99%) were purchased from Sigma Aldrich. Allura Red AC (ARAC, MW = 496.42 g mol^{-1}) was purchased from Tokyo Chemical Industry Co., Ltd. Dimethylformamide (DMF, 99.5%) and methanol were supplied by Fisher Scientific. Hexane (HPLC) and dichloromethane (HPLC, 99%) were supplied by J.T. Baker. Ethanol (99.8%) was purchased from VWR Chemicals and acetone (99%) was purchased from Aik Moh Paints & Chemicals Pte Ltd. Commercial polypropylene membrane filters (pore size: 0.1 μm) were supplied by Sterlitech. All materials were used as received unless otherwise specified.

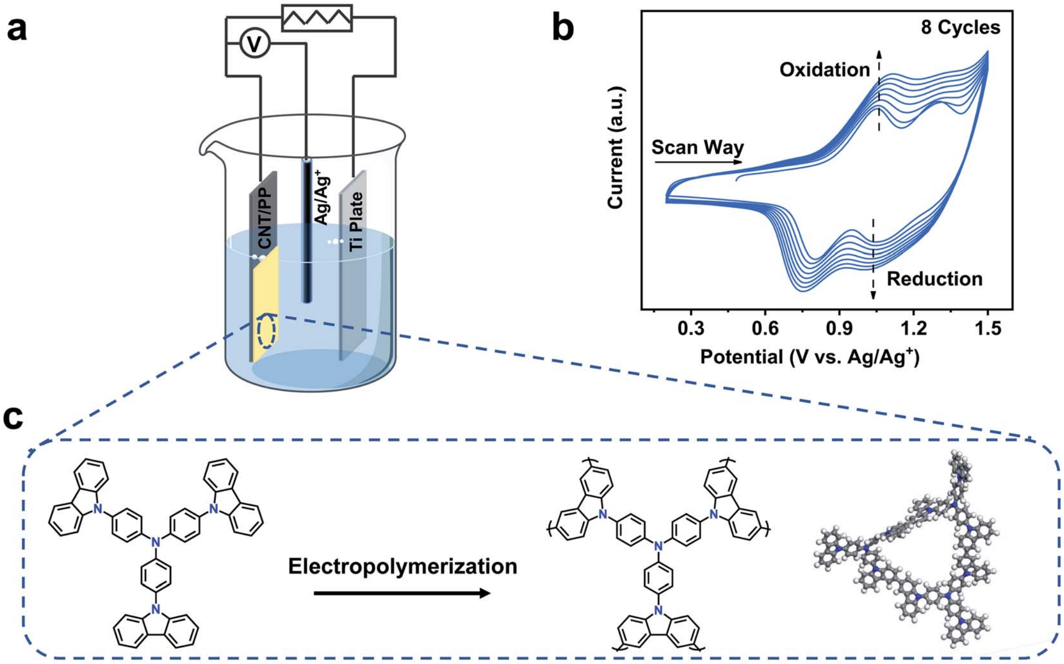

Fig. 1 (a) An illustration of the three-electrode electrochemical cell used for TCTA polymerization on the CNT/PP film. (b) Multicycle cyclic voltammetry profiles of TCTA with the scanning potential from 0.2 to 1.5 V *vs.* Ag/Ag$^+$, at a scan rate of 50 mV s^{-1}. (c) A schematic representation of the electrochemical polymerization of TCTA-EP films and their elementary pore structures.

2.2. Characterization methods

The membrane surface and cross section were observed by field emission scanning electron microscopy (FESEM JEOL JSM-7610F). The surface roughness of membranes was measured by using an atomic force microscope (AFM, Agilent Technologies, Santa Clara, CA). The chemical structure of the monomer and membrane was analyzed by Fourier-transform infrared spectroscopy (FTIR, Bruker Tensor 27 FTIR) and X-ray photoelectron spectroscopy (XPS, Kratos AXIS Ultra DLD, Kratos Analytical Ltd., England) with a Mono Al Kα X-ray source ($h\nu = 1486.71$ eV, 5 mA, and 15 kV (75 Watt)). The angle of the detector and samples surface was set to 90°. Before analysis, all XPS spectra were calibrated by fixing C 1s (C–C bond) at 284.6 eV. N_2 sorption isotherms were recorded at 77 K using a surface area and pore size analyzer (Micromeritics ASAP 2460). Prior to measurement, the polymer samples were degassed at 395 K for 24 h. A SurPASS electrokinetic analyzer (Anton Paar 57GmbH, Austria) was applied to measure the zeta potential of the membrane surface. The water contact angle (WCA) of the membranes was measured by using a Goniometer (VCA Optima, AST Products Inc.). Thermogravimetric analysis (TGA) was conducted on a thermal gravity analyzer (Bruker Tensor 27 FTIR) in a nitrogen atmosphere at a heating rate of 10 °C min^{-1}. Transmission electron microscopy (TEM) images were obtained by field emission transmission electron microscopy (FETEM, JEOL JEM-2100F).

2.3. Fabrication of the CNT/PP membrane

SWCNT dispersion was prepared by adding 8 mg SWCNT powder and 400 mg SDS into 200 mL deionized water and then ultrasonicated for 4 h by using a probe sonicator under 40 W. To remove the undispersed SWCNTs, the SWNT dispersion was further centrifuged at 10 000 rpm for 1 h. The CNT/PP supporting membrane was then prepared by filtering 10 mL of the collected SWCNT supernatant onto commercial polypropylene with an effective diameter of 35 mm. The prepared CNT/PP substrate was washed with deionized water and then dried overnight at 60 °C under vacuum and their morphology is shown in Fig. 2a.

2.4. Electrochemical synthesis of the TCTA-EP membrane

The electrochemical synthesis of TCTA was performed by using a three-electrode system attached to an electrochemical workstation (AUTOLAB, PGSTAT302N). The CNT/PP supporting membrane, Ag/AgCl electrode and titanium metal plate were used as the working, reference and counter electrodes, respectively. The electrolyte solution was prepared by dissolving TCTA monomer (0.296 mg mL^{-1}) and tetrabutylammonium perchlorate (0.1 M) as supporting electrolytes in a mixture of dichloromethane, acetonitrile and propylene carbonate (2.5/0.9/1.6, v/v/v). Cyclic voltammetry (CV) was conducted in the range between 0.2 and 1.5 V at a scan rate of 50 mV s^{-1}. After the predefined CV cycles, the as-synthesized membranes were immersed in a mixture of dichloromethane, acetonitrile and propylene carbonate to completely remove the supporting electrolytes and any unreacted monomers followed by drying overnight at 60 °C under vacuum. The as-prepared TCTA-EP membranes were used to evaluate their OSN performance.

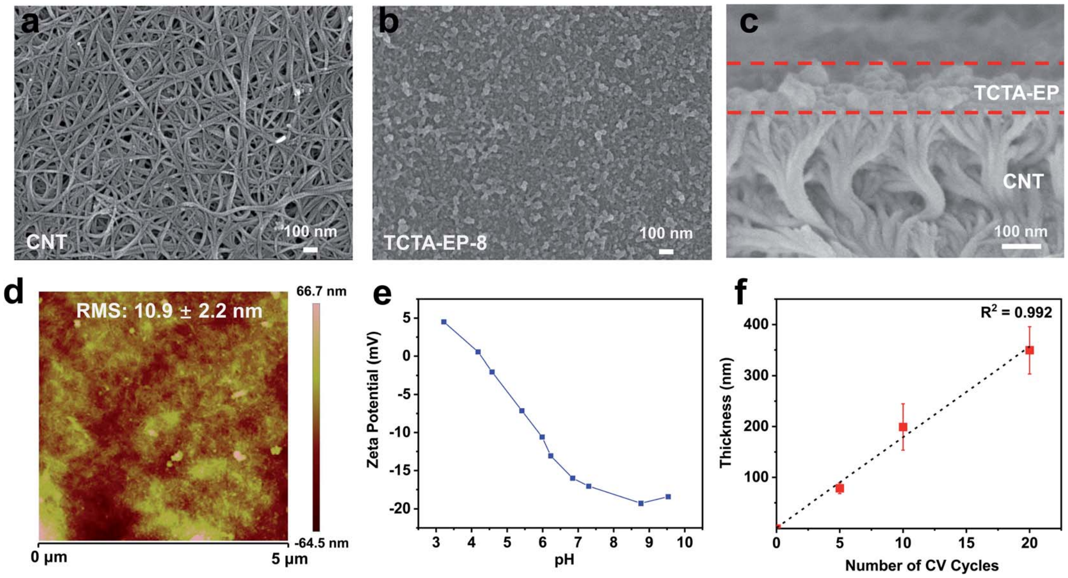

Fig. 2 SEM images of (a) the CNT/PP film, (b) surface morphology of the TCTA-EP-8 membrane and (c) cross section of the TCTA-EP-8 membrane. (d) AFM image of the TCTA-EP-8 membrane. (e) Surface zeta potential of the TCTA-EP-8 membrane. (f) Average thickness of the TCTA-EP layer *versus* the CV cycle number.

2.5. Evaluation of membrane separation properties

Pressure-driven OSN performance was evaluated *via* a homemade dead-end cell with a suspending stirrer to reduce the concentration polarization. The pressure on the feed side driven by N_2 gas was set to 6 bar and the feed solutions were maintained at room temperature (~22 °C) unless otherwise specified. The solute rejection was tested using a series of feed solutions containing solutes with various molecular weights and charges (Table S1†). The effective area of the membrane was around 0.196 cm^2 sealed by an O-ring in the dead-end cell unless otherwise specified. The cross-flow performance of the membrane was evaluated *via* a lab-built cross-flow setup equipped with a tandem filtration cell. The effective membrane area in the cell was 3.14 cm^2. The applied pressure and crossflow velocity were kept at 6 bar and 130 m s^{-1} respectively during the measurements. Before the collection of permeate, the membranes were preconditioned with solvent under 6 bar until the system reached a stable state. Solvent permeance (J, L m^{-2} h^{-1} bar^{-1}) was calculated as:

$$J = V/(A \times t \times p) \tag{1}$$

where V is the permeate volume (L) calculated by dividing the permeate weight by the solvent density. A is the effective testing membrane area (m^2), t is the operating time (h) for permeate collection and p is the applied pressure (bar). The solute rejection (R_i, %) was calculated by using the following formula:

$$R_i = (1 - (C_{P,i}/C_{F,i})) \times 100\% \tag{2}$$

where $C_{F,i}$ and $C_{P,i}$ represent the solute concentrations in feed and permeate solutions, respectively. The feed solute concentration was 50 ppm unless otherwise specified. The solute concentrations of the feed and permeate solutions were quantified by using a UV-Vis spectrometer (Agilent Technologies, Cary 60). Error bars represent SDs for at least two batches of membranes with the same parameters for each data point.

2.6. Membrane stability under harsh conditions

To investigate the chemical stability of the TCTA-EP membrane under harsh conditions, membranes were immersed in 1.8 M H_2SO_4 in water, 1.4 M NaOH in water and 0.9 M triethylamine in DMF respectively for 7 days. After immersion, the TCTA-EP membranes were rinsed with deionized water to remove the residual solution mixture for morphology and chemical structure characterization. The OSN performance of TCTA-EP membranes under harsh conditions was investigated through strong basic solutions (0.9 M triethylamine in DMF with 50 ppm Allura Red AC) under different temperatures.

3. Results and discussion

3.1. Electrochemical synthesis of TCTA-EP membranes and characterization

In principle, EP is carried out in a three-electrode cell connected with an electrochemical workstation.[44] The working electrode (WE) where electrochemical polymerization occurs contains monomer solution and the supporting electrolyte. The WE is usually composed of well conductive and chemically inert materials. The other two electrodes, reference electrode (RE) and counter electrode (CE), serve as a reference for the standard electrode potential and component of the current loop, respectively.[40] The electrosynthesis of the TCTA-EP film was conducted by multicycle cyclic voltammetry (CV) in a three-electrode electrochemical cell (Fig. 1a). Before the polymerization, CNTs were pre-deposited on a PP substrate in order to enhance the conductivity of the substrate. CNTs were chosen due to their good conductivity, large surface area, and potentially high porosity when assembled into a thin layer. The CNTs-PP film then acts as the WE to induce the polymerization of TCTA. During the polymerization, a half reaction of redox reaction occurs at the working electrode, while the other half reaction occurs at the counter electrode, where protons are reduced to form hydrogen gas.[45] Fig. 1b shows the multistage oxidation and reduction in the corresponding CV curve. In the anodic sweep, a shoulder at $\sim$0.68 V and oxidative potential at $\sim$1.05 emerge, which were fully reversible from the triphenylamine core,[46] as presented in the mechanism in Fig. S1.†[47] Another oxidative peak at 1.28 V is assigned to the oxidation of peripheral carbazole and induced cross-linking.[46] In addition, it is observed that the oxidation and reduction currents rise gradually with increasing cycle number, indicating the gradual growth of the TCTA-EP film. The TCTA-EP films fabricated at different CV cycle numbers are denoted as TCTA-EP-*X*, where *X* is the CV cycle number.

As the polymerization proceeded, a continuous TCTA-EP film with a highly crosslinked structure was formed on the CNT/PP support whose CNT layer is about $\sim$740 nm thick, as observed in the SEM images (Fig. 2b, c and S2†). The TCTA-EP-8 film presents a smooth surface morphology with a root-mean square (RMS) roughness of 10.9 nm (Fig. 2d) and negatively charged surface (-13.07 to -17.06 mV) in the pH range of 6.2 to 7.3 (Fig. 2e). The number of CV scan cycles is one of the important electropolymerization parameters that affect the membrane morphology and thickness. We see that the surface roughness of the TCTA-EP films increases with the increased scan cycles (Fig. S3†) and it is possible to precisely control the film thickness *via* simply adjusting the scan cycles (Fig. S4†). Fig. 2f plots the average thickness *versus* the CV cycle number, showing a linear dependence of film thickness on the CV cycle number. The chemical structure of the TCTA-EP film was characterized by FTIR and XPS analysis. The FTIR spectra of the TCTA monomer (Fig. 3a) present two vibration peaks at $\sim$720 and $\sim$748 cm^{-1}, which are assigned to the 1,2-bisubstituted benzene ring in carbazole and benzene, respectively.[46] The polymerization of the TCTA monomer is confirmed by the dramatically weakened signal of bisubstituted benzene rings and a newly generated characteristic peak of the trisubstituted benzene ring at about 803 cm^{-1}, indicating the formation of dimeric carbazoles (insert of Fig. 3a).[46] The electrolyte doping levels of the TCTA-EP films were determined from XPS spectra (Fig. 3b). In the XPS spectra of the TCTA-EP-8 film, Cl 2p, as the signal of the electrolyte (tetrabutylammonium perchlorate), is not detected by the instrument, indicating negligible electrolyte doping and high purity of TCTA-EP films. Furthermore, the microporosity of

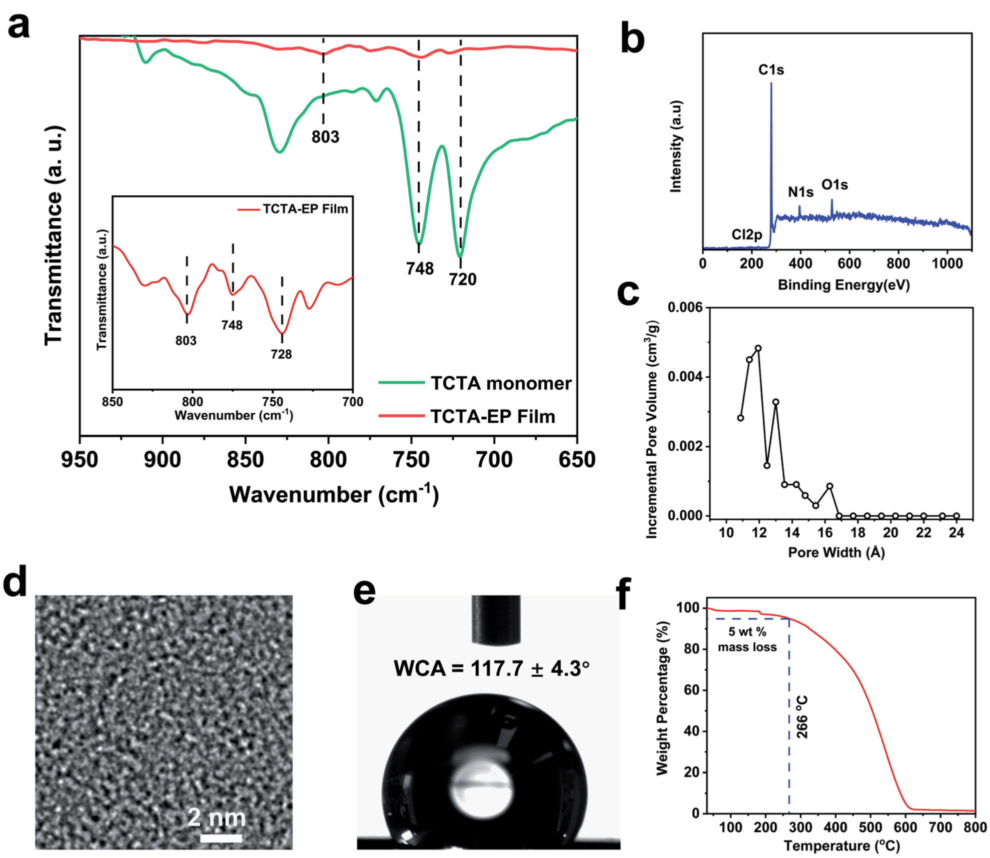

Fig. 3 Chemical and structural characterization of the TCTA-EP-8 membrane: (a) FTIR spectra of the TCTA monomer and TCTA-EP-8 membrane. (b) XPS spectra, (c) pore-size distribution profiles calculated using nonlocal density functional theory (NLDFT), (d) TEM image, (e) water contact angle (WCA) and (f) TGA curve.

TCTA-EP films was probed by nitrogen physisorption (Fig. S5†), and the pore-size distribution (Fig. 3c) presents a main peak at ~10 Å. Randomly distributed micropores with an average pore size of around 1 nm are observed in the TEM image (Fig. 3d and S6†) of the TCTA-EP films. The water contact angle (WCA) of the TCTA-EP-8 film is 117.7 ± 4.3° (Fig. 3e), indicating its hydrophobic nature compared to that of the CNT/PP support (77.8 ± 1.8°, Fig. S7†). Fig. 3f shows the temperature-dependent weight loss profile of TCTA-EP powder, where a 5% weight loss onset temperature is found at around 266 °C, which suggests that the film can be safely applied for separation below 266 °C.

3.2. Molecular sieving of TCTA-EP membranes in OSN

The molecular sieving capability of the TCTA-EP membranes was investigated in dead-end cells with various organic solvents and solutes with different chemical functionalities and structures (Tables S1 and S2, ESI Note I†). Fig. 4a presents the impacts of the CV cycle number on the rejection and permeance of the TCTA-EP membranes. The DMF permeance of the TCTA-EP membranes decreases from 88.9 to 3.8 L m^{-2} h^{-1} bar^{-1} with the CV cycle number increasing from 5 to 15, which is consistent with the membrane thickness. The rejection of Allura Red AC (496.42 g mol^{-1}) is ~77.9% at 5 cycles and thereafter increases to > 95%, indicating the formation of a defect-free cross-linked network structure. TCTA-EP-10 and TCTA-EP-15 permeances are too low to be practically helpful. Therefore, TCTA-EP-8 was chosen for further study as it shows a balanced permeation of 19.6 L ± 3.1 m^{-2} h^{-1} bar^{-1} and a rejection of 96.0 ± 0.6%. We then fabricated TCTA-EP-8 membranes with a larger area (Fig. S8†). The largest TCTA-EP film that we fabricated reaches an area of ~9.62 cm^2, limited by the size of CNT working electrodes fabricated in the lab. The large TCTA-EP-8 membrane presents a rejection of 92.6 ± 1.3% for Allura Red AC. The slight decline of the rejection compared to that of the membrane with a small area (96.0 ± 0.6%) may be due to the limited conditions for upscaling in the lab (*e.g.* the small three-electrode electrochemical cell may lead to uneven deposition of the CMPs on the large CNT/PP support).

Fig. 4b presents the permeance of various organic solvents across the TCTA-EP-8 membrane. A linear relationship (R^2 = 0.93) is seen when permeance is plotted against the inverse of solvent viscosity 1/η (Fig. 4b). Moreover, the correlations between solvent permeance and Hansen solubility parameters or the diameter of the solvents are nonlinear (R^2 lower than 0.3) (Fig. S9†), indicating that these factors might not affect solvent transport. Besides, we found that the product of permeance and viscosity is a constant, independent of Hansen solubility parameters (Fig. S10†), suggesting that the solvent transport in TCTA-EP membranes follows the pore-flow model.[48,49] Acetone, with a viscosity (0.306 mPa s) smaller than that of ethanol (1.081 mPa s), had higher permeance than ethanol, although they are all polar solvents and have comparable kinetic diameters (Table S2†). Because of the abundant carbon and nitrogen atoms in the polymer chains and the relative hydrophobicity, the TCTA-EP-8 membrane shows high permeance of both apolar hexane (60.1 L m^{-2} h^{-1} bar^{-1}) and polar acetone (56.8 L m^{-2} h^{-1} bar^{-1}). This is different from hydrophilic polyamide-based membranes,

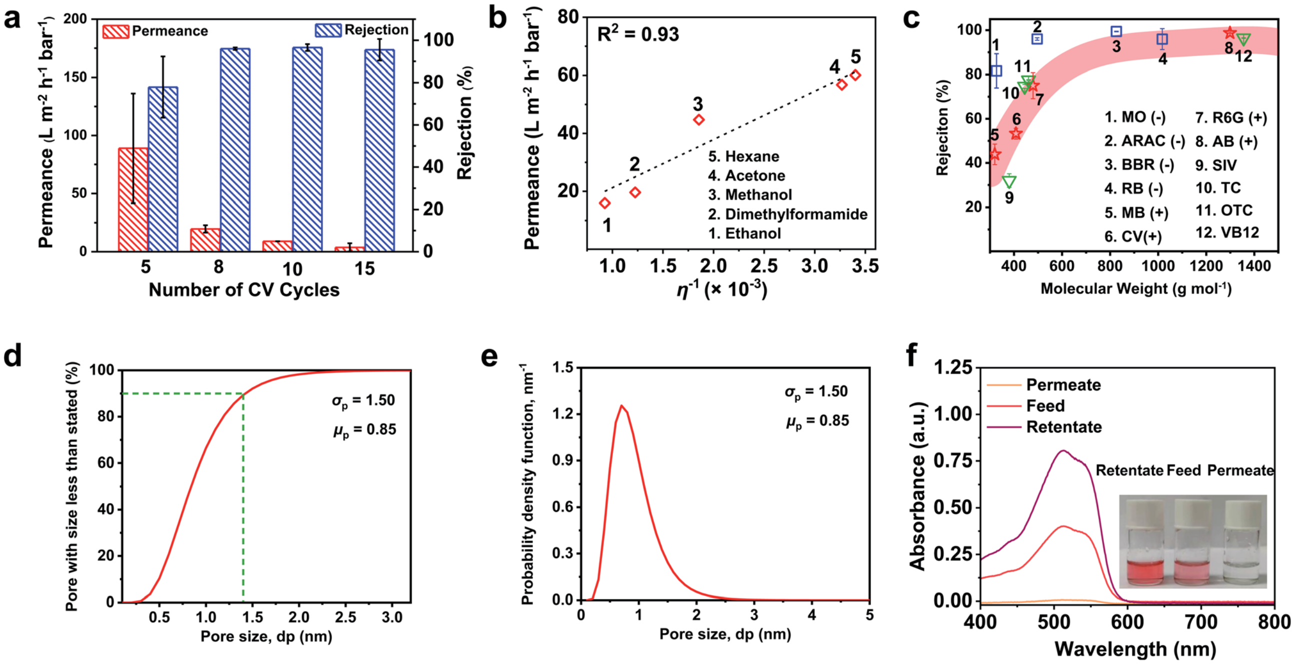

Fig. 4 (a) Rejection and permeance of TCTA-EP films with different CV cycle numbers. The feed solution was 50 ppm Allura Red AC (MW = 496.42 g mol^{-1}) in DMF. (b) The organic solvent permeance of the TCTA-EP-8 membrane against the inverse of viscosity. (c) Rejection of the TCTA-EP-8 film towards different dyes and pharmaceutical molecules in DMF. (d) Cumulative pore size distribution curves and (e) probability density function curves of the TCTA-EP-8 membrane. (f) UV absorption spectra of the feed, permeate and retentate after 50 mL permeate was collected from the 100 mL feed with the TCTA-EP-8 membrane. The feed solution was 50 ppm Allura Red AC (MW = 496.42 g mol^{-1}) in DMF.

making TCTA-EP membranes favorable for OSN applications over a wide range of solvents.

Next, a selection of different solutes whose molecular weight spans from 300 to 1400 g mol^{-1} was applied to evaluate the separation performance of the TCTA-EP-8 membrane, including positively and negatively charged dyes, and pharmaceutical molecules. Fig. 4c plots the solute rejection *versus* molecular weight. A clear size-dependent rejection is observed when neutral solutes including Sudan IV (380.44 g mol^{-1}), tetracycline (444.43 g mol^{-1}), and vitamin B$_{12}$ (1355.37 g mol^{-1}) were used. Similar trends are seen with the positively charged dyes. In general, the rejection experiences a sharp rise in the molecular weight range of 400 to 500 g mol^{-1}. At the molecular weights of ~1000–1200 g mol^{-1}, the rejection is >95% for all types of solutes. The cumulative pore size distributions and probability density function curves were obtained from the rejections of neutral solutes (ESI Note II†) as presented in Fig. 4d and e, respectively. We see that the mean of effective pore size (μ_p) is 0.84 nm and 90% of the pores have a size less than 1.4 nm. Moreover, the geometric standard deviation of the TCTA-EP-8 membrane ($\sigma_p = 1.5$) is smaller than that of common polymeric nanofiltration membranes ($\sigma_p = \sim 3$),[50] and comparable to that of reported nanofiltration membranes ($\sigma_p = \sim 1.2$), which have be applied for sub-1 Å precision separation,[51] indicating the narrow pore size distributions of the TCTA-EP-8 membrane.

In addition, the TCTA-EP-8 membrane presents charge selectivity for solutes with similar molecular weights. The rejection of oxytetracycline (neutral molecule, 460.46 mol^{-1}) and Rhodamine 6G (cationic molecule, 479.02 g mol^{-1}) is 77.5 ± 0.3% and 75.0 ± 5.6%, respectively, whereas Allura Red AC (anionic molecule, 496.42 g mol^{-1}) is largely retained (96.0 ± 0.6%). This is well explained by the electrostatic interactions between solutes and the negatively charged membrane.[52] In order to further exclude the effects of solute adsorption on the rejection, we conducted mass balance calculations of solute molecules in the feed, permeate and retentate.[53] 100 mL feed solution containing 50 ppm Allura Red AC in DMF was filtered through the TCTA-EP-8 membrane. After 50 mL permeate was collected, the UV absorption intensity of Allura Red AC in the retentate is about two times larger than that of the feed solution, and the permeate is clean without a significant solute peak (Fig. 4f). Hence, it confirms the negligible adsorption of dyes within the membrane. An adsorption test was further conducted to exclude the contribution of adsorption effects on rejections (ESI Note III†).

3.3. Membrane stability under harsh conditions

The rigid cross-linked structure endows the TCTA-EP membrane with extraordinary chemical stability in various solvents, chemical reagents and high pressure and temperature, which is critical to address current challenges in real OSN applications under extreme conditions. The excellent long-term stability of the TCTA-EP-8 membrane is signified by the stable rejection of aggressive DMF solution containing a high solute concentration (500 ppm Allura Red AC) for around 200 h (Fig. 5a). A slight decline of the permeance is found during the long-term test, possibly due to the fouling issue. Various operating pressures up to 30 bar were applied and we see that ethanol flux increases linearly with operating pressure ($R^2 = 0.988$) (Fig. 5b) without affecting the rejection of Allura Red AC (Fig. 5c). The framework stability of the membrane is crucial for commercial pressure-driven membrane separation processes, especially under cross-flow conditions which exert higher shear stress compared to that of dead-end filtration mode. Some 2D membranes such as graphene oxide (GO) formed by vacuum filtration, drop/dip-coating and evaporation methods usually suffer from the delamination of nanosheets under high surface stress, which will lead to failure under cross-flow mode.[54] We therefore evaluated the separation performance of the TCTA-EP-8 membrane in cross-flow mode under a linear flow rate of 130 m s^{-1}. The compaction of the TCTA-EP-8 membrane is observed (Fig. S13†) and the DMF permeance declines in the first few hours and then reaches a steady state with a DMF permeance of ~25 L m^{-2} h^{-1} bar^{-1} (Fig. S14†) and stable rejection of Allura Red AC for 24 h (Fig. S15†).

The solvent stability and the separation performance of the TCTA-EP membrane were further evaluated at different temperatures up to 100 °C. The DMF permeance increases with the temperature (Fig. 5d) and reaches 33.1 ± 1.2 L m^{-2} h^{-1} bar^{-1} at 100 °C, which is much higher than that shown in most previous literature research (Table S3†). To understand the mechanism, we calculated the permeance (P_T) at temperature T based on the DMF permeance at 25 °C (P_{25}) and the change of viscosity η at temperature T as shown in the following equation:[12]

$$P_T = P_{25} \times \frac{\eta_{25}}{\eta} \tag{3}$$

As shown in Fig. 5d, the experimental permeance shows similar trends to the calculated values suggesting the important role of reduced viscosity in the temperature-dependent permeance. Other factors including the energy barrier, effective intrapore viscosity, and sorption/desorption phenomenon may also affect the transport process.[15,55] Meanwhile, the rejection of Allura Red AC remains almost constant. It slightly declines to 94.4 ± 2.2% at 100 °C (Fig. 5e), likely due to the lower energy barrier for solute transport at higher temperature.[28]

The solvent and acid/base resistance of the membrane are a major challenge for practical OSN applications.[56] Three solvent systems based on commercial processes were chosen to explore the possibility of TCTA-EP-8 membranes in industry-relevant processes. 1.8 M H_2SO_4 in water and 1.4 M NaOH in water were chosen to investigate their stability in strong acid and base aqueous solutions that have been applied to tackle the potential fouling problems. The third one mirrors the common reaction conditions used in the fabrication of active pharmaceutical ingredients (APIs), which contain 0.9 M triethylamine in DMF.[57] TCTA-EP-8 membranes were first immersed in 1.8 M H_2SO_4 in water, 1.4 M NaOH in water and 0.9 M triethylamine in DMF respectively for 7 days. The morphology and chemical structure of these membranes remained almost unchanged

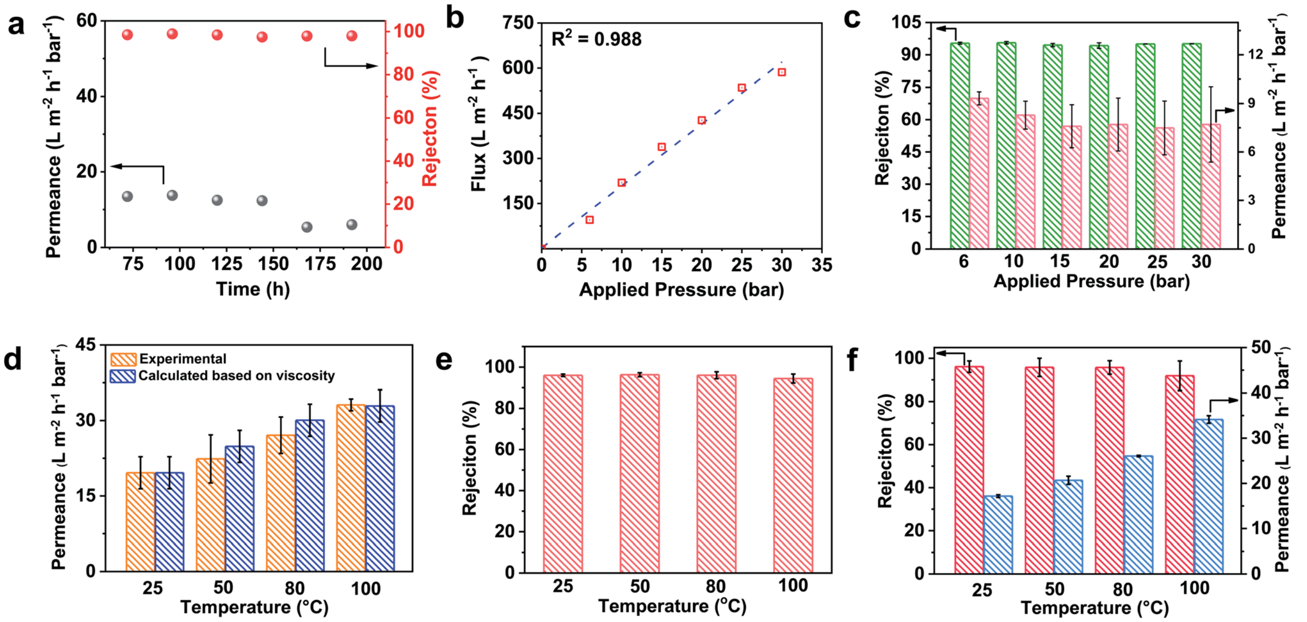

Fig. 5 (a) Long-term performance of the TCTA-EP-8 membrane. The feed solution was 500 ppm Allura Red AC (MW = 496.42 g mol^{-1}) in DMF. (b) Pure ethanol flux and (c) rejection of Allura Red AC of the TCTA-EP-8 membrane under different applied pressures. The feed solution was 50 ppm Allura Red AC (MW = 496.42 g mol^{-1}) in ethanol. (d) Experimental permeance and calculated permeance based on eqn (3) through the TCTA-EP-8 membrane *versus* operation temperature. The feed solution was 50 ppm Allura Red AC (MW = 496.42 g mol^{-1}) in DMF. The viscosity at different temperature was calculated based on previous literature.[47] (e) The rejection of 50 ppm Allura Red AC (MW = 496.42 g mol^{-1}) in DMF by the TCTA-EP-8 membrane *versus* operation temperature. (f) The rejection of Allura Red in DMF containing a high base content by the TCTA-EP-8 membrane *versus* operation temperature. The feed solution was 50 ppm Allura Red AC (MW = 496.42 g mol^{-1}) in DMF containing 0.9 M triethylamine.

based on SEM images (Fig. S16†) and FTIR results (Fig. S17†). The OSN performance of the TCTA-EP-8 membranes was further evaluated in DMF solution containing a high base content of triethylamine at different temperatures (Fig. 5f). Specifically, 50 ppm Allura Red AC in DMF with 0.9 M triethylamine was used as the feed solution. The rejection of Allura Red AC remains over 90% (Fig. 5f), indicating the remarkable stability and robust porous structure of TCTA-EP membranes.

4. Conclusions

In this work, TCTA-EP membranes have been successfully fabricated through an electropolymerization process. By simply adjusting the CV scan cycles, the film thickness could be precisely controlled. The membrane was found to be microporous with a pore size of ~10 Å, smooth and negatively charged. The optimal TCTA-EP-8 membrane displayed a high permeance of apolar solvent (hexane) of 60.1 L m^{-2} h^{-1} bar^{-1} and polar solvent (acetone) of 56.8 L m^{-2} h^{-1} bar^{-1}. In addition, the membrane showed molecular sieving properties towards pharmaceutical molecules and charged dyes. The permeance reached 33.1 ± 1.2 L m^{-2} h^{-1} bar^{-1} at >94.4% rejection of Allura Red in DMF at 100 °C. Moreover, due to its rigid cross-linked structure, the TCTA-EP membrane has demonstrated excellent stability in high pressure and high temperature DMF with strong bases. Overall, these extraordinary properties make TCTA-EP membranes promising candidates for challenging separation involving organic solvents.

Author contributions

Yanqiu Lu, Wei Liu, and Sui Zhang designed the research; Yanqiu Lu performed the research; Kaiyu Wang contributed to the cross-flow test. Yanqiu Lu, Wei Liu, and Sui Zhang analysed the data; the original draft was prepared by Yanqiu Lu, and was reviewed, validated and edited by Sui Zhang.

Conflicts of interest

There are no conflicts to declare.

Acknowledgements

The authors acknowledge the financial support from the Cambridge Centre for Carbon Reduction in Chemical Technology Phase 2 (C4T2, A-0005328-01-00) and Ministry of Education of Singapore (A-0009181-00-00). We would also like to thank Prof. Siowling Soh (National University of Singapore) for sharing the use of the electrochemical workstation.

References

1 P. Marchetti, M. F. Jimenez Solomon, G. Szekely and A. G. Livingston, *Chem. Rev.*, 2014, **114**, 10735–10806.
2 R. K. Henderson, C. Jiménez-González, D. J. Constable, S. R. Alston, G. G. Inglis, G. Fisher, J. Sherwood, S. P. Binks and A. D. Curzons, *Green Chem.*, 2011, **13**, 854–862.

3 Z.-Y. Wang, R. Feng, W.-J. Wang, Y.-X. Sun, S.-N. Tao, Y.-M. Wang, Y.-F. Chen, Z.-J. Fu, X.-L. Cao and S.-P. Sun, *Adv. Membr.*, 2021, **1**, 100007.

4 L. Nie, K. Goh, Y. Wang, J. Lee, Y. Huang, H. E. Karahan, K. Zhou, M. D. Guiver and T.-H. Bae, *Sci. Adv.*, 2020, **6**, eaaz9184.

5 D. B. Shinde, G. Sheng, X. Li, M. Ostwal, A.-H. Emwas, K.-W. Huang and Z. Lai, *J. Am. Chem. Soc.*, 2018, **140**, 14342–14349.

6 P. Vandezande, L. E. Gevers and I. F. Vankelecom, *Chem. Soc. Rev.*, 2008, **37**, 365–405.

7 R. P. Lively and D. S. Sholl, *Nat. Mater.*, 2017, **16**, 276–279.

8 S. Hermans, H. Mariën, C. Van Goethem and I. F. Vankelecom, *Curr. Opin. Chem. Eng.*, 2015, **8**, 45–54.

9 H. B. Park, J. Kamcev, L. M. Robeson, M. Elimelech and B. D. Freeman, *Science*, 2017, **356**, eaab0530.

10 Y. Lu, W. Liu, J. Liu, X. Li and S. Zhang, *Adv. Membr.*, 2021, **1**, 100014.

11 D. Zhao, J. F. Kim, G. Ignacz, P. Pogany, Y. M. Lee and G. Szekely, *ACS Nano*, 2019, **13**, 125–133.

12 J. da Silva Burgal, L. Peeva and A. Livingston, *J. Membr. Sci.*, 2017, **525**, 48–56.

13 L. Peeva, J. da Silva Burgal, S. Vartak and A. G. Livingston, *J. Catal.*, 2013, **306**, 190–201.

14 P. J. Harrington, *Pharmaceutical Process Chemistry for Synthesis: Rethinking the Routes to Scale-Up*, John Wiley & Sons, 2011.

15 H. Saidani, N. B. Amar, J. Palmeri and A. Deratani, *Langmuir*, 2010, **26**, 2574–2583.

16 N. Ben Amar, H. Saidani, A. Deratani and J. Palmeri, *Langmuir*, 2007, **23**, 2937–2952.

17 M. J. Snow, D. de Winter, R. Buckingham, J. Campbell and J. Wagner, *Desalination*, 1996, **105**, 57–61.

18 M. Y. Jeon, D. Kim, P. Kumar, P. S. Lee, N. Rangnekar, P. Bai, M. Shete, B. Elyassi, H. S. Lee and K. Narasimharao, *Nature*, 2017, **543**, 690–694.

19 P. Kumar, D. W. Kim, N. Rangnekar, H. Xu, E. O. Fetisov, S. Ghosh, H. Zhang, Q. Xiao, M. Shete and J. I. Siepmann, *Nat. Mater.*, 2020, **19**, 443–449.

20 S. Kandambeth, B. P. Biswal, H. D. Chaudhari, K. C. Rout, S. Kunjattu H, S. Mitra, S. Karak, A. Das, R. Mukherjee and U. K. Kharul, *Adv. Mater.*, 2017, **29**, 1603945.

21 J. Liu, G. Han, D. Zhao, K. Lu, J. Gao and T.-S. Chung, *Sci. Adv.*, 2020, **6**, eabb1110.

22 S. Yuan, X. Li, J. Zhu, G. Zhang, P. Van Puyvelde and B. Van der Bruggen, *Chem. Soc. Rev.*, 2019, **48**, 2665–2681.

23 F. Alduraiei, S. Kumar, J. Liu, S. P. Nunes and G. Szekely, *J. Membr. Sci.*, 2022, **648**, 120345.

24 D. Ma, G. Han, Z. F. Gao and S. B. Chen, *ACS Appl. Mater. Interfaces*, 2019, **11**, 45290–45300.

25 J. Campbell, R. Davies, D. C. Braddock and A. Livingston, *J. Mater. Chem. A*, 2015, **3**, 9668–9674.

26 S. Zhou, Y. Zhao, J. Zheng and S. Zhang, *J. Membr. Sci.*, 2019, **591**, 117347.

27 J. Gao, S. Japip and T.-S. Chung, *Chem. Eng. J.*, 2018, **353**, 689–698.

28 Y. Lu, L. Zhang, L. Shen, W. Liu, R. Karnik and S. Zhang, *Proc. Natl. Acad. Sci. U. S. A.*, 2021, **118**, e2111360118.

29 L. Shen, Q. Shi, S. Zhang, J. Gao, D. C. Cheng, M. Yi, R. Song, L. Wang, J. Jiang and R. Karnik, *Sci. Adv.*, 2021, **7**, eabg6263.

30 C. Cheng, S. A. Iyengar and R. Karnik, *Nat. Nanotechnol.*, 2021, **16**, 989–995.

31 B.-Y. Guo, S.-D. Jiang, M.-J. Tang, K. Li, S. Sun, P.-Y. Chen and S. Zhang, *J. Phys. Chem. Lett.*, 2019, **10**, 4609–4617.

32 J. Ran, P. Zhang, C. Chu, P. Cui, X. Ai, T. Pan, Y. Wu and T. Xu, *J. Membr. Sci.*, 2020, **602**, 117963.

33 B. Liang, H. Wang, X. Shi, B. Shen, X. He, Z. A. Ghazi, N. A. Khan, H. Sin, A. M. Khattak and L. Li, *Nat. Chem.*, 2018, **10**, 961–967.

34 X. He, H. Sin, B. Liang, Z. A. Ghazi, A. M. Khattak, N. A. Khan, H. R. Alanagh, L. Li, X. Lu and Z. Tang, *Adv. Funct. Mater.*, 2019, **29**, 1900134.

35 Z. Zhou, X. Li, D. Guo, D. B. Shinde, D. Lu, L. Chen, X. Liu, L. Cao, A. M. Aboalsaud and Y. Hu, *Nat. Commun.*, 2020, **11**, 1–9.

36 J. Gong, R.-B. Lin and B. Chen, *Chem*, 2018, **4**, 2269–2271.

37 Y. Xu, S. Jin, H. Xu, A. Nagai and D. Jiang, *Chem. Soc. Rev.*, 2013, **42**, 8012–8031.

38 P. Lindemann, M. Tsotsalas, S. Shishatskiy, V. Abetz, P. Krolla-Sidenstein, C. Azucena, L. Monnereau, A. Beyer, A. Gölzhäuser and V. Mugnaini, *Chem. Mater.*, 2014, **26**, 7189–7193.

39 M. Zhang, X. Jing, S. Zhao, P. Shao, Y. Zhang, S. Yuan, Y. Li, C. Gu, X. Wang and Y. Ye, *Angew. Chem., Int. Ed.*, 2019, **58**, 8768–8772.

40 H. Ma, Y. Chen, X. Li and B. Li, *Adv. Funct. Mater.*, 2021, **31**, 2101861.

41 Z. Zhou, D. Guo, D. B. Shinde, L. Cao, Z. Li, X. Li, D. Lu and Z. Lai, *ACS Nano*, 2021, **15**, 11970–11980.

42 D. Guo, X. Li, F. Ming, Z. Zhou, H. Liu, M. N. Hedhili, V. Tung, H. N. Alshareef, Y. Li and Z. Lai, *Nano Energy*, 2020, **73**, 104769.

43 S. Guan, W. Wang, B. Li, J. Zheng and C. Xu, *J. Mater. Chem. C*, 2019, **7**, 7520–7524.

44 Q. Zhang, H. Dong and W. Hu, *J. Mater. Chem. C*, 2018, **6**, 10672–10686.

45 C. Li, H. Bai and G. Shi, *Chem. Soc. Rev.*, 2009, **38**, 2397–2409.

46 Y. Liang, C. Liu, M. Zhao, R. Wang, D. Zhang, C. Wang, L. Zhou, L. Wang, Z. Xie and J. Peng, *ACS Appl. Mater. Interfaces*, 2020, **12**, 20714–20721.

47 C.-W. Kuo, J.-K. Chang, Y.-C. Lin, T.-Y. Wu, P.-Y. Lee and T.-H. Ho, *Polymers*, 2017, **9**, 543.

48 Q. Yang, Y. Su, C. Chi, C. Cherian, K. Huang, V. Kravets, F. Wang, J. Zhang, A. Pratt and A. Grigorenko, *Nat. Mater.*, 2017, **16**, 1198–1202.

49 J. G. Wijmans and R. W. Baker, *J. Membr. Sci.*, 1995, **107**, 1–21.

50 G.-E. Chen, Y.-J. Liu, Z.-L. Xu, Y.-J. Tang, H.-H. Huang and L. Sun, *RSC Adv.*, 2015, **5**, 40742–40752.

51 Y. Liang, Y. Zhu, C. Liu, K.-R. Lee, W.-S. Hung, Z. Wang, Y. Li, M. Elimelech, J. Jin and S. Lin, *Nat. Commun.*, 2020, **11**, 1–9.

52 D. Hua and T.-S. Chung, *Carbon*, 2017, **122**, 604–613.

53 A. He, Z. Jiang, Y. Wu, H. Hussain, J. Rawle, M. E. Briggs, M. A. Little, A. G. Livingston and A. I. Cooper, *Nat. Mater.*, 2022, 1–8.

54 W.-H. Zhang, M.-J. Yin, Q. Zhao, C.-G. Jin, N. Wang, S. Ji, C. L. Ritt, M. Elimelech and Q.-F. An, *Nat. Nanotechnol.*, 2021, **16**, 337–343.

55 T. Tsuru, S. Izumi, T. Yoshioka and M. Asaeda, *AIChE J.*, 2000, **46**, 565–574.

56 I. B. Valtcheva, S. C. Kumbharkar, J. F. Kim, Y. Bhole and A. G. Livingston, *J. Membr. Sci.*, 2014, **457**, 62–72.

57 L. Peeva, J. Arbour and A. Livingston, *Org. Process Res. Dev.*, 2013, **17**, 967–975.